Supporting Information

Sub-nanometer mapping of the interfacial electric field profile using a vibrational Stark shift ruler

Dhritiman Bhattacharyya,[a] Pablo E. Videla,[b] Joseph M. Palasz,[c] Isaac Tangen,[a] Jinhui Meng,[a] Clifford P. Kubiak,*[c] Victor S. Batista,*[b] and Tianquan Lian*[a]

[a]Department of Chemistry, Emory University, 1515 Dickey Drive Northeast, Atlanta, Georgia 30322, USA. E-mail: tlian@emory.edu

[b]Department of Chemistry and Energy Sciences Institute, Yale University, 225 Prospect Street, New Haven, Connecticut 06520, USA. E-mail: victor.batista@yale.edu

[c]Department of Chemistry and Biochemistry, University of California, San Diego, 9500 Gilman Drive, MC 0358, La Jolla, California, 92093, USA. E-mail: ckubiak@ucsd.edu

Experimental details:

I. Synthesis of PDI-$W(CO)_5$:

All chemicals and solvents were used as received unless otherwise noted. 1,4-phenylenediisocyanide (PDI) was purchased from Sigma Aldrich and stored cold under nitrogen. Tetrahydrofuran (THF) and dichloromethane (DCM) were purified on an alumina column under argon atmosphere in a Grubbs-style solvent purification system and further dried over 3Å molecular sieves. All synthetic protocols were conducted in a glovebox with a nitrogen atmosphere.

Following previously reported protocols with slight modifications,[1] $W(CO)_6$ (1g, 2.84 mmol) and tetrabutylammonium chloride (0.789 g, 2.84 mmol) were stirred in THF (10mL) overnight at 23 ^{o}C. The resulting yellow solution was evaporated to dryness in-vacuo, redissolved in MeOH (10 mL) and filtered. To the yellow filtrate was added a solution of 1,4 phenylene

diisocyanide (0.619 mg, 4.83 mmol) in MeOH (5 ml) and the mixture was stirred for 4 hours until a brown-yellow precipitate formed. The mixture was filtered, and the solid was collected and dried under vacuum to yield $W(CO)_5(CN\text{-}C_6H_4\text{-}NC)$ (abbreviated as PDI-$W(CO)_5$) as a yellow/brown solid (0.553 mg, 43% yield). As a solid the complex is stable under ambient conditions on the week to month timescale, however effort was made to limit the compounds exposure to UV light. ^{13}C NMR, FTIR and UV/Vis were consistent with the literature preparation. Additionally, the ^{1}H NMR spectrum of the aryl region of PDI-$W(CO)_5$ was recorded in DMSO-d_6 (Figure S1) to further verify the absence of dimeric PDI$[W(CO)_5]_2$ or unmetallated PDI.

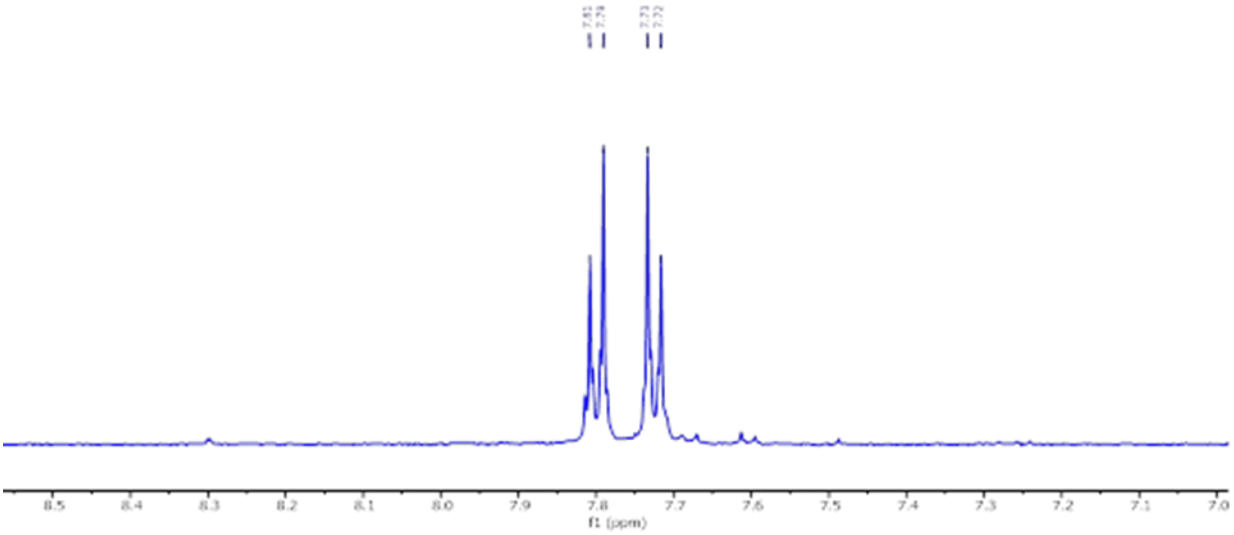

Figure S1. Aryl region of the ^{1}H NMR of $W(CO)_5$PDI in DMSO-d_6 taken on a Jeol JNM-ECA 500 MHz instrument showing the second order AA′BB′ multiplet characteristic of the asymmetric 1,4-diisocyanobenzene ligand.

II. Monolayer preparation:

To prepare a monolayer of PDI-$W(CO)_5$, gold coated (1000 Å thickness) microscope slides were purchased from Substrata Thin Film Solutions. The vendor uses a thin 2-7 nm layer of chromium (99.99%) as an adhesion promoter for all gold coatings onto borosilicate glass slides.

The gold slides were sonicated with water, methanol and again with water to remove any organic impurity that might contaminate the surface. The clean gold slides were then soaked overnight into 10 mM solution of PDI-$W(CO)_5$ in DCM. Before performing the VSFG experiment, one gold slide was taken out of the sample solution, rinsed, and sonicated for 3 mins in DCM to remove all unattached molecules from the surface and dried thoroughly.

III. Electrochemical VSFG set-up:

The SFG setup in the Lian laboratory is based on a 7W, 1-kHz, 60-fs Ti:sapphire 800-nm laser system. Approximately 2W was directed, by use of a beam-splitter, to an optical parametric amplifier (OPA), not used in this experiment. The remaining 5W was split, with 4W directed to an IR OPA producing tunable IR pulses and 1W to a home-built 4f stretcher, which gives us a ~7 cm^{-1} (FWHM) 800-nm beam. VSFG experiments were performed by overlapping a femtosecond broadband IR pulse (center frequency ~ 2050 cm^{-1}, FWHM ~ 300 cm^{-1}, pulse energy: 10 μJ) and a picosecond narrowband 800 nm visible pulse (FWHM ~ 7 cm^{-1}, pulse energy: 6 μJ) at the sample both spatially and temporally; with incident angles of 59° and 65° with respect to the surface normal, respectively; and the reflected VSFG signal at the phase matching direction was collimated and refocused onto the slit of an 300 mm monochromator (Acton Spectra-Pro 300i, 1200 grooves/mm and 750-nm blaze grating) and detected with a liquid nitrogen-cooled CCD (Princeton Instruments, PyLoN, 1340×100 pixels) operating at –120 °C. The details of our electrochemical VSFG spectrometer can be found in our previous publications.[2-3] The VSFG spectra reported in this work were measured at PPP polarization combination, where the polarizations of the SFG, visible and IR beams were all P polarized and conventionally written from left to right.[4] Each spectrum was measured in the accumulation mode for 15 seconds.

For electrochemical measurements, a glass dish placed in a plastic chamber was used as electrochemical cell (Fig. S2). The SAM-modified Au slide was attached by conducting copper tape (isolated from the electrolyte by epoxy) and served as working electrode, whereas the Ag/Ag^+ electrode and a Pt wire were used as reference electrode and counter electrode, respectively; and all of them were connected to a potentiostat (Gamry Instruments) in a three-terminal configuration. A 0.2 M solution of tetrabutylammonium hexafluorophosphate ($TBAPF_6$) in DCM was used as an electrolyte solution. To ensure efficient electrolyte (mass) transport during our electrochemistry experiment, a 25 μm Teflon spacer was placed on top of the Au surface; above which a 2 mm thick CaF_2 window was pressed down in contact. The SAMs were found to be stable in the potential range between 0 V and -0.9 V vs Ag/Ag^+ electrode. The molecules can be stripped off from the Au surface when the potential is outside this window. After the SFG measurement, the molecules were removed from the Au surface by applying negative potential (usually –1.8 V) for 1 min (The bubbles were removed from the thin layer by adjusting the CaF_2 window). The SFG signal from the bare Au surface was recorded as the reference spectrum (the IR intensity profile) which is used to normalize the VSFG spectra of the SAM on the Au surface as a function of potential. A schematic diagram of our VSFG experiment under electrochemical condition, and the current-voltage (CV) behavior of PDI-$W(CO)_5$ SAM on Au (0.2 M $TBAPF_6$ in DCM, Ag/Ag^+ reference electrode, and Pt counter electrode) are shown in Figure S2.

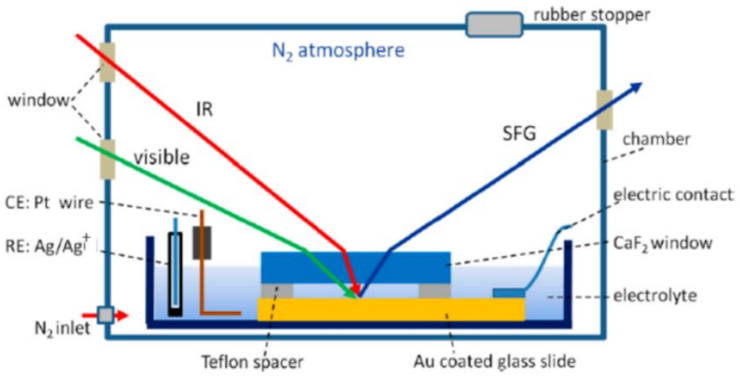

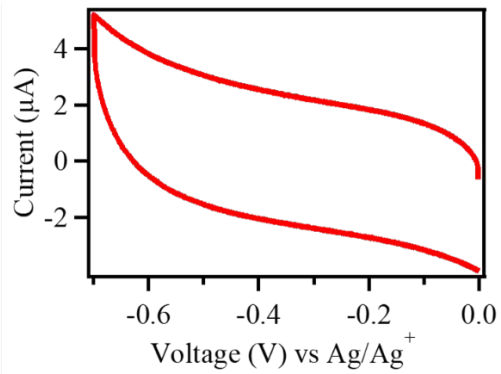

Figure S2. (left) Schematic diagram of our electrochemical VSFG experimental set-up. (right) Current-voltage (CV) plot of PDI-$W(CO)_5$ SAM on Au under electrochemical condition, as described in the text.

IV. SHINER and solution Raman measurement:

Shell-isolated nanoparticle-enhanced Raman (SHINER) spectroscopy is particularly valuable to acquire high quality Raman signals on various well-defined substrates, without the need of surface-roughening. The key advantage of the shell-isolated nanoparticles (SHIN) is their uniform and ultrathin SiO_2 shell, which permits the Au core to generate strong electromagnetic nearfields and simultaneously protects it from the chemical environment. The details of the SHIN preparation can be found in a publication by Li et al.,[5] and the SHINER spectrum of PDI-$W(CO)_5$ SAM on Au is shown in Figure S3. For this measurement, we have used a HeNe laser producing a 632.8 nm continuous source (Thorlabs, HNL210LB) of average power 5 mW focused on the sample using a 10X microscope objective (10X Olympus Plan Achromat Objective, 0.25 NA, 10.6 mm WD, Thorlabs, RMS10X). The average power of the laser was adjusted to avoid sample damage. SHINERS signals were collected by the objective, filtered using a dichroic mirror and a long pass filter, dispersed by an imaging spectrograph (Shamrock, Andor, 600 G/mm grating) and detected by an electron-multiplied charge coupled device (Newton EMCCD, Andor). Individual SHINERS spectrum was acquired with a 30 second integration time.

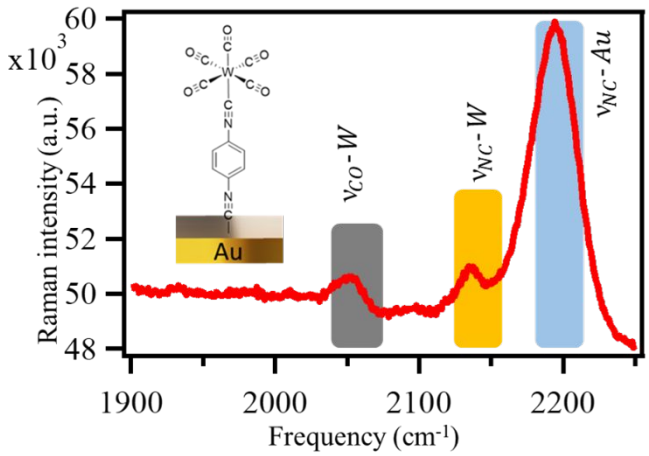

Figure S3. Shell-isolated nanoparticle enhanced Raman (SHINER) spectrum of PDI-$W(CO)_5$ SAM on a planar gold surface.

The SHINERS spectrum of PDI-$W(CO)_5$ SAM on Au shows three Raman active modes of the molecule; however, the ~2000 cm^{-1} mode is absent. As shown by Burdett et al.,[6] molecules of general form $M(CO)_5L$ (M=metal, L=ligand) belongs to C_{4v} point group symmetry; the ~2000 cm^{-1} mode corresponds to a B_1 type vibration and is Raman active. According to our theoretical calculation, this mode should demonstrate weak Raman activity as well. To verify this, we have measured the solution Raman spectrum of PDI-$W(CO)_5$ dissolved in DCM as shown in Figure S4. For the solution-phase Raman spectra, a confocal Raman spectrometer (HORIBA, LabRam HR Evolution) equipped with a 532 nm laser was used with the LabSpec 8 software. For both the DCM background and the analyte sample, ca. 5 mL of the appropriate solution was transferred into a borosilicate glass petri dish and focused under the microscope. The 1800 grooves per millimeter setting was used to obtain spectra with 10 second acquisition times for 5 accumulations. The solution spectrum clearly shows a weak Raman active mode around ~2000 cm^{-1}, as predicted by our calculation. Given its weak Raman activity, we believe that the Raman enhancement of the mode is not enough to show up in the SHINERS spectrum. On the other hand, VSFG technique

being inherently surface-selective with sub-monolayer sensitivity can easily probe this mode with high signal to noise ratio. It is to be noted that in the high frequency region (>2100 cm^{-1}), there is only one peak observed in the solution Raman spectrum corresponding to the NC-W coupled vibration. The Raman activity of the free NC mode is very weak, and it likely gets masked within the shoulder of the NC-W vibration.

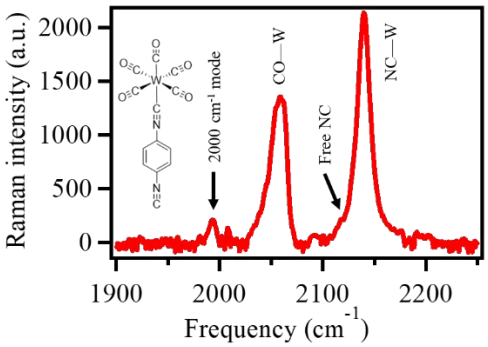

Figure S4. Solution Raman spectrum of 5 mM PDI-$W(CO)_5$ in DCM.

V. UV-VIS measurement:

The UV-VIS absorption spectrum of the complex was measured on a Shimadzu UV-3600 spectrophotometer with a 40 µM solution of PDI-$W(CO)_5$ in DCM in a 1 cm pathlength cuvette. As evident, MLCT transition of this molecule appears below 400 nm, therefore, the lights used in our Raman (632.8 nm) and VSFG (800 nm) experiments cannot directly excite the molecule in its higher electronic states, avoiding light-induced dissociation (photodegradation).

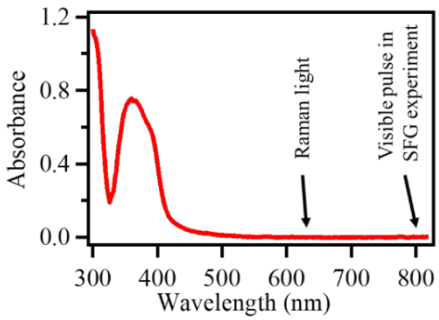

Figure S5. UV-VIS spectrum of a 40 μM solution of PDI-$W(CO)_5$ in DCM in a 1 cm pathlength cuvette.

Sample stability:

The -$W(CO)_5$ complexes, in general, are photoactive and often undergo CO loss. Aqueous solvents, containing dissolved oxygen, is not good for the long-term stability of the sample. As a result, our VSFG experiment was performed in organic solvent (DCM), and the electrolyte solution was purged with Argon for 30 mins before the experiment. We have used an 800 nm visible laser beam for our VSFG measurement. It is important to note that a 515 nm visible pulse which can barely excite the MLCT transition of PDI-$W(CO)_5$ molecules (see Fig. S5), is sufficient to induce photodegradation, although very little. So, it is imperative to carefully choose light wavelengths to study these molecules spectroscopically.

Computation details:

Density functional theory (DFT) calculations were carried out following our previous study of PDI on gold.[7] We used the ωB97XD functional[8] along with a cc-pVTZ[9] basis set for light atoms and LANL2DZ,[10-12] which utilizes an effective core potential, for W and Au, as implemented in the Gaussian 2016 software suite of programs.[13] The gold surface was modelled as a cluster, consisting of a 7+3 two-layer Au(111) surface with a lattice parameter of 4.16 Å (see Figure S6). For the geometry optimizations, the gold atoms were kept fixed and angular constraints were applied to keep the PDI moiety perpendicular to the surface. All calculations included solvent effects (DCM) through the polarizable continuum model (PCM).[14] Unless otherwise state, all frequencies reported were scaled by 0.95.

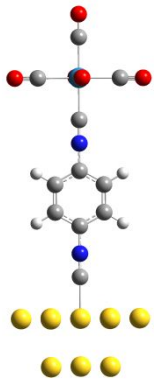

Figure S6. Cluster model of PDI-$W(CO)_5$ attached to the gold surface used in DFT calculations.

In Figure S7, we present the DFT-based IR and Raman (harmonic) spectra of the PDI-$W(CO)_5$ molecule in solution and attached to a gold surface in the spectral region of study, as in our present work. In Figure S8, we present the main normal mode displacements associated with these transitions. The $W(CO)_5$-PDI molecule contains 7 vibrational modes in the spectral region 1900-2250 cm^{-1}, corresponding to W-CO and NC stretches. The two highest frequency modes can be assigned to fairly localized NC-W and NC-Au vibrations. We remark that when unbound from gold (namely, in solution), the now-free NC stretching mode shift down to 2134 cm^{-1} (see Figure S7). The 5 remaining vibrational modes correspond to W-CO stretching, with different degrees of delocalization between axial and equatorial CO (see below). Note that due to the symmetry of the $W(CO)_5$, the low frequency modes that are IR-active, are Raman-inactive and vice-versa, making these modes SFG-inactive. Note that the mode at ~1934 cm^{-1} presents a very small Raman activity in our calculations but is negligible when compared to the other Raman-active modes (Figure S7) and should be undetected in the VSFG spectra. On the other hand, the W-CO, NC-W and NC-Au modes located at 2048 cm^{-1}, 2149 cm^{-1} and 2188 cm^{-1}, respectively, show considerable IR and Raman activity and are predictive to be VSFG active.

To characterize the extent of (de)localization of each normal mode, we compute the contribution of each atom to the normal mode displacement. Table S1 shows the atomic contribution. Note that the highest frequency mode is entirely localized on the NC group bound to Au, whereas the ~2150 cm^{-1} and ~2050 cm^{-1} modes are somewhat mixed, but the former has a predominant contribution from N≡C—W coupled vibration, whereas the latter is mostly localized on W-bound equatorial carbonyl groups. The rest of the vibrational modes can be assigned to stretching modes involving delocalized equatorial or axial CO motifs.

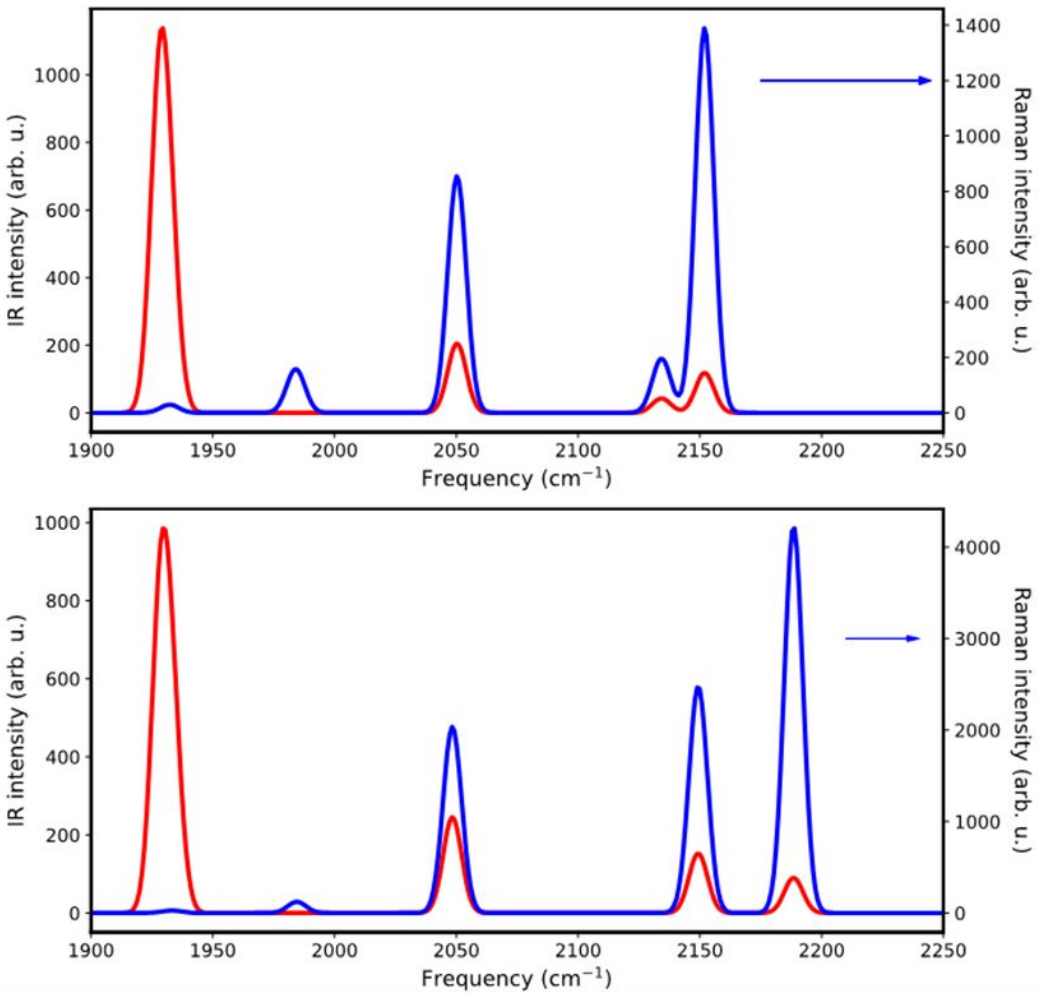

Figure S7. DFT-based IR (Red) and Raman (Blue) spectra of PDI-$W(CO)_5$ in solution (top panel) and attached to the gold surface (bottom panel).

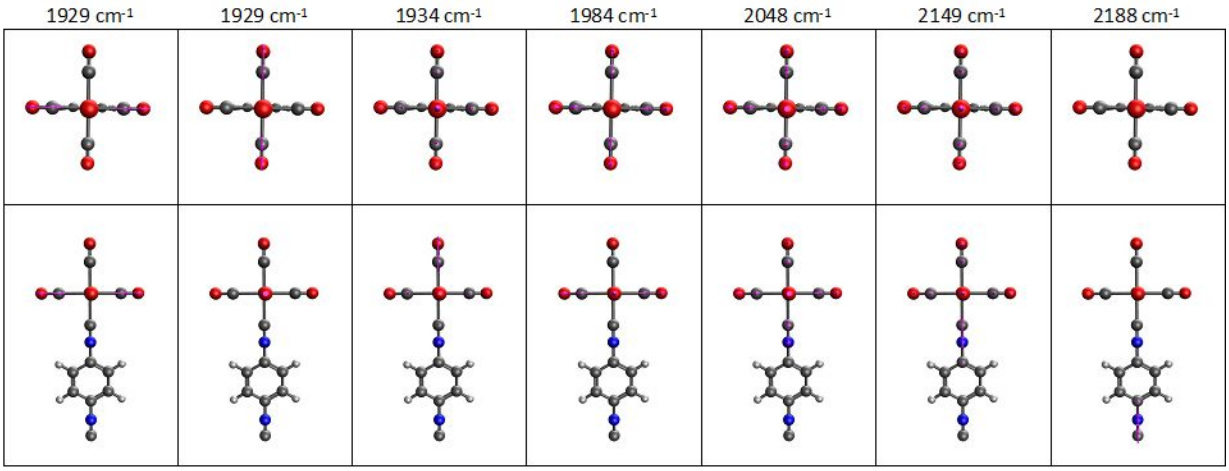

Figure S8. Top view (top panels) and side view (bottom panels) of normal mode displacements of relevant vibrational modes of $W(CO)_5$-PDI bound to gold. Gold atoms are not shown for clarity. We remark that the localized Au-NC mode at 2188 cm^{-1}, has a frequency of 2134 cm^{-1} in solution.

Table S1. Relative atomic contribution of normal modes in PDI-$W(CO)_5$ bound to gold.

Mode frequency (cm^{-1})	CO (equatorial)	CO (axial)	NC-W	NC-Au
1929	100%	-	-	-
1929	100%	-	-	-
1934	8%	90%	2%	
1984	100%	-	-	-
2048	72%	3%	25%	-
2149	20%	6%	72%	-
2188	-	-	-	99%

The vibrational Stark tuning rate ($\Delta\mu$) was calculated by performing optimizations of the molecule on the gold cluster in the presence of a uniform electric field aligned perpendicular to the gold cluster's face, oriented along the Au-C metal-molecule both in the positive and negative directions. From the optimized structures, we performed harmonic frequencies calculations in the presence of an applied field to compute vibrational frequencies as a function of the field. The Stark tuning rate ($\Delta\mu$) was obtained from linear fits to the dependence of the frequency with the field.

To test the error associated with the DFT model in the Stark tuning rate, we performed additional calculations for the $W(CO)_5$-PDI molecule on the gold cluster using the PBE0 functional,[15] as well as calculations for a bare PDI molecule on gold. Table S2 summarizes the results. We remark that, besides the NC-W mode that shows the biggest difference (~50%), there is little influence (<1%) of the functional used on $\Delta\mu$. Note that both DFT models show the same qualitative trends between PDI and $W(CO)_5$-PDI molecules, namely the susceptibility of the free NC mode is increased by ~3-4 times when the $W(CO)_5$ is attached.

Table S2. Dependence of Stark tuning rate ($\Delta\mu$) on DFT functional.

Molecule	DFT Model[(a)]	$\Delta\mu$ [cm^{-1}/(V/nm)]		
PDI		NC-Au	Free NC	
	ωB97XD	9.8	-5.1	
	PBE0	12.8	-4.2	
PDI-$W(CO)_5$		NC-Au	NC-W	CO-W
	ωB97XD	10.4	-19.5	-17.8
	PBE0	11.9	-11.7	-17.7

[(a)] Basis set: cc-pVTZ[9]/LANL2DZ[10-12].

Simulations of DFT-based SFG spectra were performed following our previously described approach.[3, 7, 16-20] Here, we only mention the details pertaining to the system under study. The SFG intensity is related to the second-order molecular hyperpolarizabilities $\beta_{ijk,q} \sim \frac{1}{\omega_q} \frac{\partial \alpha_{ij} \partial \mu_k}{\partial Q_q \partial Q_q}$, where α_{ij} and μ_k are elements of the polarizability tensor and dipole moment, respectively, and Q_q is the normal coordinate of the q-th vibrational mode with frequency ω_q. Vibrational parameters were obtained at the DFT level using the cluster model as detailed above. Azimuthal symmetry of the PDI-$W(CO)_5$ on gold was assumed and the hyperpolarizability tensor was averaged over the azimuthal angle. Following the surface dipole selection rule on metallic

interfaces, PPP spectra were computed by only considering the $\beta_{zzz,q}$ tensor element. In the theoretical calculations, nonresonant contributions were neglected (namely, $A_{NR} = 0$).

Spectral fitting procedure:

To extract the frequencies of different vibrational modes of the surface-bound PDI-W(CO)$_5$ molecules, we fit the experimental VSFG spectrum using the following equation:[21]

$$I_{VSFG} = \left| A_{NR} e^{i\Delta} + \sum_k \frac{b_k \Gamma_k}{\omega_{IR} - \omega_k + i\Gamma_k} \right|^2 \qquad (1)$$

where ω_{IR} stands for the frequency of the IR pulse. The second order susceptibility of each normal mode is modeled using a Lorentzian, with b_k, ω_k, and Γ_k representing the amplitude, frequency, and linewidth, respectively, of mode k. A_{NR} is the amplitude of the second order susceptibility of the metallic surface, referred to as non-resonant response. In homodyne detected VSFG spectroscopy, the resonant molecular and non-resonant Au responses interfere with each other, with Δ being the relative phase between them.[22] Four Lorentzians, corresponding to NC-Au, NC-W, CO-W, and the Fermi resonance mode, were used to fit the VSFG spectrum of the PDI-W(CO)$_5$ SAM on Au (Figure 1b). A similar procedure using two Lorentzians was used to fit the VSFG spectrum of PDI on gold shown in Figure 1c. These fitting parameters are listed in Table S3.

Table S3. VSFG spectral fitting parameters corresponding to Figure 1b (PDI-W(CO)$_5$) and Figure 1c (PDI), as shown in the main text.

	NC bound to Au			Free NC			Nonresonant signal	
PDI	b_k	ω_k	Γ_k	b_k	ω_k	Γ_k	A_{NR}	φ
	-0.75	2172.1	24.5	0.07	2124.6	8.4	-0.66	320

	NC bound to Au			NC-W			Nonresonant signal	
	b_k	ω_k	Γ_k	b_k	ω_k	Γ_k	A_{NR}	φ
	-22.7	2186.5	13.7	19.9	2142.0	13.3	-1.03	321
PDI-W(CO)$_5$	CO-W			Fermi Resonance mode				
	b_k	ω_k	Γ_k	b_k	ω_k	Γ_k		

	18.9	2057.5	15.9	7.4	2004.6	12.9	

Table S4. Fitting parameters of the VSFG spectra as a function of applied potential (Figure 2a).

	Frequency (cm^{-1})			
	NC-Au	NC-W	CO-W	Fermi resonance
0.0V	2195.2 ± 0.52	2142.3 ± 0.174	2057.5 ± 0.205	2002.9 ± 0.218
-0.1V	2193.0 ± 0.421	2142.8 ± 0.178	2058.0 ± 0.216	2002.7 ± 0.234
-0.2V	2190.3 ± 0.370	2143.1 ± 0.192	2058.3 ± 0.224	2002.7 ± 0.252
-0.3V	2187.6 ± 0.307	2143.2 ± 0.224	2058.6 ± 0.251	2002.9 ± 0.278
-0.4V	2186.0 ± 0.386	2142.9 ± 0.197	2058.3 ± 0.228	2004.3 ± 0.223
-0.5V	2184.3 ± 0.305	2143.1 ± 0.214	2058.5 ± 0.236	2004.4 ± 0.223
-0.6V	2182.9 ± 0.276	2143.5 ± 0.230	2058.6 ± 0.241	2004.2 ± 0.253
-0.7V	2180.4 ± 0.278	2143.7 ± 0.304	2058.8 ± 0.283	2003.9 ± 0.293
-0.8V	2177.8 ± 0.252	2144.0 ± 0.535	2058.6 ± 0.376	2003.7 ± 0.361

Calculating the interfacial electric field as a function of potential.

The interfacial electric field can be correlated to the potential dependent frequency of the vibrational probes, as follows:

$$\omega(\varphi) = \omega_0 + \overrightarrow{\Delta\mu}.\vec{F}(\varphi) \qquad (2)$$

where, $\vec{F}(\varphi)$ is bias-dependent electric field strength, ω_0 and $\omega(\varphi)$ stand for the vibrational frequencies in the absence of applied voltage and at potential φ, respectively. $\overrightarrow{\Delta\mu}$ is known as Stark

tuning rate, representing the susceptibility of a vibrational probe towards applied electric field and can be calculated by taking the difference in the dipole moments between the ground and excited vibrational states. Taking the derivative of the above expression gives rise to the following equation.

$$\frac{dF(\varphi)}{d\varphi} = \frac{1}{\Delta\mu}\frac{d\omega(\varphi)}{d\varphi} \qquad (3)$$

The absolute electric field strength as a function of applied voltage ($F(\varphi)$), can be deduced by integrating equation 3 as shown in the following:

$$\int_{\varphi_{PZC}}^{\varphi} dF(\varphi) = \frac{d\omega(\varphi)}{d\varphi}.\frac{1}{\Delta\mu}.\int_{\varphi_{PZC}}^{\varphi} d\varphi \qquad (4)$$

$$F(\varphi) - F(\varphi_{PZC}) = \frac{d\omega(\varphi)}{d\varphi}.\frac{1}{\Delta\mu}.(\varphi - \varphi_{PZC}) \qquad (5)$$

$$F(\varphi) = \frac{d\omega(\varphi)}{d\varphi}.\frac{1}{\Delta\mu}.(\varphi - \varphi_{PZC}) \qquad (6)$$

φ_{PZC} represents the potential of zero charge (PZC) of Au/SAM/electrolyte system. At PZC, the electric field strength is assumed to be zero, i.e., $F(\varphi_{PZC}) = 0$. φ_{PZC} depends on various factors including the type of electrolyte solution (organic or aqueous), ionic strength of the electrolyte, the nature of the SAM decorated on the electrode surface and most importantly, the crystal structure of the electrode.[23-26] Potential of zero charge (PZC) of an Au/SAM/electrolyte system can be experimentally determined from the minimum of the potential-dependent capacitance plot or from second harmonic generation (SHG) spectroscopy where potential-dependent non-resonant signal intensity goes through a minimum at PZC.[3, 19] Unfortunately, the PDI-$W(CO)_5$ SAM is stripped

off from the Au surface once the potential goes positive of 0.0 V vs Ag/Ag^+, barring us from direct experimental determination of its PZC.

Simulation of electric field and electric potential.

I. Gouy-Chapman (GC) model: The expression of electric field and electric potential in an electrochemical double layer can be obtained by solving Poisson-Boltzmann equation, as detailed in Bard and Faulkner's book.[27] For symmetric 1:1 electrolyte (one anion and one cation, both with charge z), the solution of Poisson-Boltzmann equation gives the expression of electric field (F), which is the negative gradient of electric potential (φ) as a function of distance from the electrode surface (x):

$$F(x) = -\frac{d\varphi}{dx} = \frac{2k_BT}{e}\kappa\sinh\left(\frac{ze[\varphi(x) - \varphi_B]}{2k_BT}\right) \quad (7)$$

where φ_B is the electric potential in the bulk, $\kappa^{-1} = \sqrt{\varepsilon\varepsilon_0 k_B T/2z^2e^2n^0}$ is the Debye length, ε is the dielectric constant of the electrolyte solution, ε_0 is the absolute permittivity, k_B is the Boltzmann constant, T is the absolute temperature, z is the absolute charge number of the ion, e is the elementary charge, and n^0 is the electrolyte concentration.[19] The Debye length is estimated to be ~ 0.23 nm, for a 0.2 M solution of $TBAPF_6$ in DCM (ε=8.93) and at room temperature (T =293 K). Integrating Eq. (7) gives rise to:

$$\tanh\left(\frac{ze[\varphi(x) - \varphi_B]}{4k_BT}\right) = \tanh\left(\frac{ze[\varphi_0 - \varphi_{PZC}]}{4k_BT}\right)e^{-\kappa x} \quad (8)$$

Here $\varphi_0 \equiv \varphi(0) - \varphi_{ref}$ is the electrode applied potential with respect to the reference electrode φ_{ref} and $\varphi_{PZC} \equiv \varphi_B - \varphi_{ref}$ is the potential of zero charge. For the Au/PDI-W(CO)5/electrolyte system we assume the PZC to be ~ -0.05 V vs Ag/Ag+. In the low potential limit, $\frac{ze\varphi}{4k_BT} < 0.5$, $\tanh\left(\frac{ze\varphi}{4k_BT}\right) \approx \frac{ze\varphi}{4k_BT}$, and equation 8 can be written as: $\varphi(x) - \varphi_B = [\varphi_0 - \varphi_{PZC}]e^{-\kappa x}$. This is a good approximation for $\varphi \leq 50/z$ mV. In the high potential limit (-0.8V, for example), the electric potential drops much more drastically (red, Figure S9) as compared to the exponentially decaying function (blue); whereas in the low potential regime (-0.1 V), the decay profiles look similar.

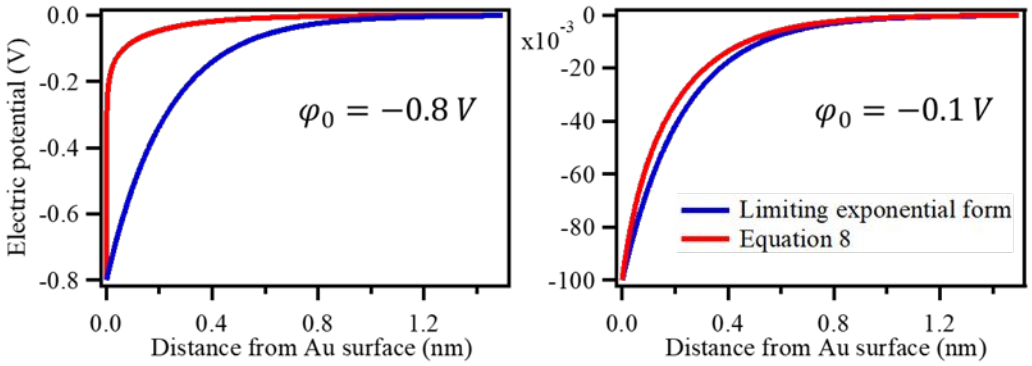

Figure S9. Electric potential as a function of distance from the Au electrode according to the GC model [Eq. 8] at high (-0.8V) and low (-0.1V) potentials, for $\kappa^{-1} = 0.23$ nm, $T = 293$ K and $\varphi_{PZC} = -0.05$ V. The limiting exponential decay (blue) is shown for comparison.

II. Gouy-Chapman-Stern (GCS) model: The GCS model assumes a Stern layer and a diffuse layer in the double-layer structure; the electric potential drops linearly within the Stern layer (φ_0 to φ_2), and in the diffuse layer it drops exponentially. Since the electric field is the gradient of electric potential, therefore, a linear drop of potential within the Stern layer results to a constant electric field. Here, we assume that the thickness of the Stern layer is x_2, as shown in Figure S10.

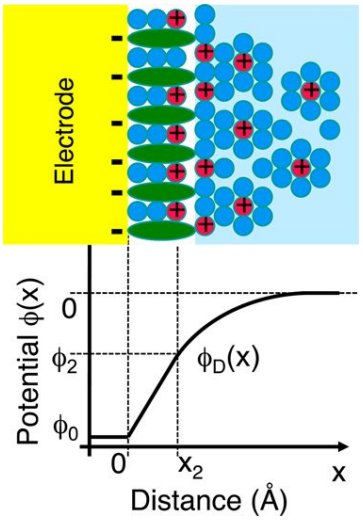

Figure S10. Top: model for Au/SAM/liquid interface. Bottom: schematic depiction of the variation of the potential across the electrode/liquid interface. Taken from Ref.[7]

Therefore, according to GCS model, the field strength experienced by the probe molecule between $x = 0$ and x_2 is constant and is given by:

$$F(x_0) = F(x_2) = -\frac{\varphi_2 - \varphi_0}{x_2} \tag{9}$$

where $\varphi_2 \equiv \varphi(x_2) - \varphi_{ref}$. The expression of electric field strength in the diffuse layer is the same as obtained for the GC model:

$$F(x) = \frac{2k_BT}{e}\kappa \sinh\left(\frac{ze[\varphi(x) - \varphi_B]}{2k_BT}\right) \quad \text{for } x \geq x_2 \tag{10}$$

Assuming the continuity of electric field at $x = x_2$, we arrive at the following expression:

$$\frac{2k_BT}{e}\kappa \sinh\left(\frac{ze[\varphi_2 - \varphi_{PZC}]}{2k_BT}\right) = -\frac{\varphi_2 - \varphi_0}{x_2} \tag{11}$$

Equation 11 can be solved numerically to obtain the value of φ_2 and $F(x_2)$. The left-hand side of equation 11 is plotted as a function of φ_2 in Figure S11 (black line), whereas the right-hand side is plotted as colored lines assuming different values of x_2, i.e., the thickness of the Stern layer. The position where these two plots intersect gives the value of φ_2 and $F(x_2)$.

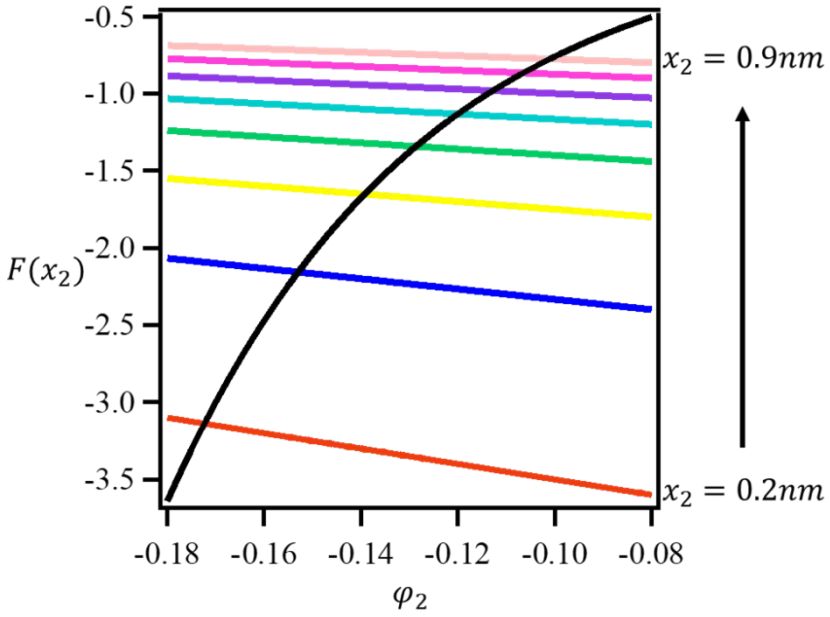

Figure S11. The left-hand side of equation 11 is plotted as a function of φ_2 (black), for $\kappa^{-1} = 0.23$ nm, $T = 293$ K and $\varphi_{PZC} = -0.05$ V. The right-hand side of equation 11 is also plotted as a function of φ_2, for φ_0=-0.8 V and different Stern layer thicknesses (x_2). The values of φ_2 and $F(x_2)$ are obtained from the corresponding values at the intersection between these two plots.

The electric potential in the Stern layer (φ_H) and the diffuse layer (φ_D) can be expressed by equations 12 and 13, respectively.

$$\varphi_H(x) - \varphi_B = \varphi_0 - \varphi_{PZC} + (\varphi_2 - \varphi_0) * \frac{x}{x_2} \tag{12}$$

$$\tanh\left(\frac{ze[\varphi_D(x) - \varphi_B]}{4k_BT}\right) = \tanh\left(\frac{ze[\varphi_2 - \varphi_{PZC}]}{4k_BT}\right)e^{-\kappa(x - x_2)} \tag{13}$$

The above expressions corresponding to the Stern layer and the diffuse layer are used to simulate the electric field and the electric potential profile within the double layer for different thicknesses of the Stern layer (x_2), as shown in the main text.

References:

1. Grubisha, D. S.; Rommel, J. S.; Lane, T. M.; Tysoe, W. T.; Bennett, D. W., Communication between metal centers in tungsten(0)-tungsten(II) complexes bridged by 1,4-diisocyanobenzene: is the ligand .pi. system involved? *Inorg. Chem.* **1992,** *31* (24), 5022-5027.
2. Bhattacharyya, D.; Videla, P. E.; Cattaneo, M.; Batista, V. S.; Lian, T.; Kubiak, C. P., Vibrational Stark shift spectroscopy of catalysts under the influence of electric fields at electrode–solution interfaces. *Chem. Sci.* **2021,** *12* (30), 10131-10149.
3. Ge, A.; Rudshteyn, B.; Videla, P. E.; Miller, C. J.; Kubiak, C. P.; Batista, V. S.; Lian, T., Heterogenized Molecular Catalysts: Vibrational Sum-Frequency Spectroscopic, Electrochemical, and Theoretical Investigations. *Acc. Chem. Res.* **2019,** *52* (5), 1289-1300.
4. Bhattacharyya, D.; Montenegro, A.; Dhar, P.; Mammetkuliyev, M.; Pankow, R. M.; Jung, M. C.; Thompson, M. E.; Thompson, B. C.; Benderskii, A. V., Molecular orientation of poly-3-hexylthiophene at the buried interface with fullerene. *J. Phys. Chem. Lett.* **2019,** *10* (8), 1757-1762.
5. Li, J. F.; Huang, Y. F.; Ding, Y.; Yang, Z. L.; Li, S. B.; Zhou, X. S.; Fan, F. R.; Zhang, W.; Zhou, Z. Y.; Wu, D. Y., Shell-isolated nanoparticle-enhanced Raman spectroscopy. *nature* **2010,** *464* (7287), 392-395.
6. Burdett, J. K.; Downs, A. J.; Gaskill, G. P.; Graham, M. A.; Turner, J. J.; Turner, R. F., Characterization by infrared and Raman spectroscopy of matrix-isolated M (CO) 5N2 (M= chromium, molybdenum, or tungsten) produced by photolysis of M (CO) 6. *Inorg. Chem.* **1978,** *17* (3), 523-532.
7. Ge, A.; Videla, P. E.; Lee, G. L.; Rudshteyn, B.; Song, J.; Kubiak, C. P.; Batista, V. S.; Lian, T., Interfacial Structure and Electric Field Probed by in Situ Electrochemical Vibrational Stark Effect Spectroscopy and Computational Modeling. *J. Phys. Chem. C* **2017,** *121* (34), 18674-18682.
8. Chai, J.-D.; Head-Gordon, M., Long-range corrected hybrid density functionals with damped atom–atom dispersion corrections. *Phys. Chem. Chem. Phys.* **2008,** *10* (44), 6615-6620.
9. Dunning Jr, T. H., Gaussian basis sets for use in correlated molecular calculations. I. The atoms boron through neon and hydrogen. *J. Chem. Phys.* **1989,** *90* (2), 1007-1023.
10. Hay, P. J.; Wadt, W. R., Ab initio effective core potentials for molecular calculations. Potentials for the transition metal atoms Sc to Hg. *J. Chem. Phys.* **1985,** *82* (1), 270-283.
11. Wadt, W. R.; Hay, P. J., Ab initio effective core potentials for molecular calculations. Potentials for main group elements Na to Bi. *J. Chem. Phys.* **1985,** *82* (1), 284-298.
12. Friesner, R. A.; Murphy, R. B.; Beachy, M. D.; Ringnalda, M. N.; Pollard, W. T.; Dunietz, B. D.; Cao, Y., Correlated ab initio electronic structure calculations for large molecules. *J. Phys. Chem. A* **1999,** *103* (13), 1913-1928.
13. Frisch, M.; Trucks, G.; Schlegel, H.; Scuseria, G.; Robb, M.; Cheeseman, J.; Scalmani, G.; Barone, V.; Petersson, G.; Nakatsuji, H., Gaussian 16 Revision C. 01, 2016. *Gaussian Inc. Wallingford CT* **2016,** *1*.
14. Tomasi, J.; Mennucci, B.; Cammi, R., Quantum mechanical continuum solvation models. *Chem. Rev.* **2005,** *105* (8), 2999-3094.
15. Adamo, C.; Barone, V., Toward reliable density functional methods without adjustable parameters: The PBE0 model. *J. Chem. Phys.* **1999,** *110* (13), 6158-6170.
16. Anfuso, C. L.; Snoeberger, R. C.; Ricks, A. M.; Liu, W.; Xiao, D.; Batista, V. S.; Lian, T., Covalent Attachment of a Rhenium Bipyridyl CO2 Reduction Catalyst to Rutile TiO2. *J. Am. Chem. Soc.* **2011,** *133* (18), 6922-6925.
17. Anfuso, C. L.; Xiao, D.; Ricks, A. M.; Negre, C. F. A.; Batista, V. S.; Lian, T., Orientation of a Series of CO2 Reduction Catalysts on Single Crystal TiO2 Probed by Phase-Sensitive Vibrational Sum Frequency Generation Spectroscopy (PS-VSFG). *J. Phys. Chem. C* **2012,** *116* (45), 24107-24114.

18. Ge, A.; Rudshteyn, B.; Psciuk, B. T.; Xiao, D.; Song, J.; Anfuso, C. L.; Ricks, A. M.; Batista, V. S.; Lian, T., Surface-Induced Anisotropic Binding of a Rhenium CO2-Reduction Catalyst on Rutile TiO2(110) Surfaces. *J. Phys. Chem. C* **2016,** *120* (37), 20970-20977.
19. Clark, M. L.; Ge, A.; Videla, P. E.; Rudshteyn, B.; Miller, C. J.; Song, J.; Batista, V. S.; Lian, T.; Kubiak, C. P., CO2 Reduction Catalysts on Gold Electrode Surfaces Influenced by Large Electric Fields. *J. Am. Chem. Soc.* **2018,** *140* (50), 17643-17655.
20. Clark, M. L.; Rudshteyn, B.; Ge, A.; Chabolla, S. A.; Machan, C. W.; Psciuk, B. T.; Song, J.; Canzi, G.; Lian, T.; Batista, V. S.; Kubiak, C. P., Orientation of Cyano-Substituted Bipyridine Re(I) fac-Tricarbonyl Electrocatalysts Bound to Conducting Au Surfaces. *J. Phys. Chem. C* **2016,** *120* (3), 1657-1665.
21. Bhattacharyya, D.; Montenegro, A.; Plymale, N. T.; Dutta, C.; Lewis, N. S.; Benderskii, A. V., Vibrational Sum Frequency Generation Spectroscopy Measurement of the Rotational Barrier of Methyl Groups on Methyl-Terminated Silicon (111) Surfaces. *J. Phys. Chem. Lett.* **2019,** *10* (18), 5434-5439.
22. Bhattacharyya, D.; Dhar, P.; Liu, Y.; Djurovich, P. I.; Thompson, M. E.; Benderskii, A. V., Vibrational Sum Frequency Generation Study of the Interference Effect on a Thin Film of 4, 4′-Bis (N-carbazolyl)-1, 1′-biphenyl (CBP) and Its Interfacial Orientation. *ACS Appl. Mater. Interfaces* **2020,** *12* (23), 26515-26524.
23. Stolberg, L.; Morin, S.; Lipkowski, J.; Irish, D., Adsorption of pyridine at the Au (111)-solution interface. *J. Electroanal. Chem. Interfacial Electrochem.* **1991,** *307* (1-2), 241-262.
24. Kolb, D.; Schneider, J., Surface reconstruction in electrochemistry: Au (100-(5× 20), Au (111)-(1× 23) and Au (110)-(1× 2). *Electrochim. Acta* **1986,** *31* (8), 929-936.
25. Cai, W.-B.; Wan, L.-J.; Noda, H.; Hibino, Y.; Ataka, K.; Osawa, M., Orientational phase transition in a pyridine adlayer on gold (111) in aqueous solution studied by in situ infrared spectroscopy and scanning tunneling microscopy. *Langmuir* **1998,** *14* (24), 6992-6998.
26. Valette, G., Hydrophilicity of metal surfaces: silver, gold and copper electrodes. *J. Electroanal. Chem. Interfacial Electrochem.* **1982,** *139* (2), 285-301.
27. Bard, A. J.; Faulkner, L. R., Fundamentals and applications. *Electrochem. Methods* **2001,** *2* (482), 580-632.